

A new *FEFF*-based wavelet for EXAFS data analysisHarald Funke,<sup>a,b\*</sup> Marina Chukalina<sup>c</sup> and Andreas C. Scheinost<sup>a,b</sup><sup>a</sup>Institute of Radiochemistry, Forschungszentrum Dresden-Rossendorf, Germany, <sup>b</sup>Rossendorf Beamline at ESRF (BM20), Grenoble, France, and <sup>c</sup>Institute of Microelectronics Technology RAS, Chernogolovka, Russia. E-mail: funke@esrf.fr

A new mother wavelet function for extended X-ray absorption fine-structure (EXAFS) data analysis has been designed, combining a model EXAFS function derived from the *ab initio* EXAFS code *FEFF*8.20 and the complex Morlet wavelet. This new *FEFF*-Morlet mother wavelet routine allows the generation of wavelets well adapted to specific EXAFS problems. A substantial gain in resolution of the wavelet ridges in  $k$  and  $r$  space is achieved. The method is applied to a structural problem of Zn–Al double-layer hydroxides, demonstrating unequivocally the homogeneity of the metal cation distribution in the hydroxide layers.

© 2007 International Union of Crystallography  
Printed in Singapore – all rights reserved**Keywords:** EXAFS; wavelet transform; data evaluation; layered double hydroxides.

## 1. Introduction

In the last five years, wavelet transform has been proven as a valuable tool in addition to classical EXAFS data analysis, especially for such structures where two types of backscattering atoms are at the same distance from the central atom (Funke *et al.*, 2005; Muñoz *et al.*, 2003). In some recent studies, wavelet analysis has been used for the interpretation of EXAFS data as well (Sahnoun *et al.*, 2007; Vespa *et al.*, 2006; Harfouche *et al.*, 2006). A short recapitulation of the wavelet transform is given in §2.

Isomorphous substitution of metal cations in minerals commonly occurs in low- $T$ , low- $P$  environments; however, it is often difficult to study using traditional EXAFS analysis. The extension of the traditional analysis by wavelet analysis is therefore well suited to investigate the short-range structure of layered double hydroxides (LDHs) or hydrotalcite minerals (Funke *et al.*, 2005). LDHs are a group of minerals hosting a wide range of divalent metal cations like  $\text{Co}^{2+}$ ,  $\text{Ni}^{2+}$ ,  $\text{Zn}^{2+}$  ( $M^{2+}$ ) (D'Espinose *et al.*, 1995). Owing to their relatively low solubility at circumneutral pH values, formation of such phases plays an important role in reducing the toxicity of metals in soils, sediments and nuclear waste repositories (Scheinost *et al.*, 1999).

LDH phases consist of layers of edge-sharing metal hydroxide octahedra, where up to one-third of the divalent cations  $M^{2+}$  are replaced by trivalent  $\text{Al}^{3+}$  (Voegelin *et al.*, 2002). The resulting net positive layer charge is compensated by hydrated anions in the interlayer space (D'Espinose *et al.*, 1995). Owing to their low crystallinity and turbostratic layer structure, LDHs are difficult to determine by X-ray diffraction. While EXAFS is much better suited for this purpose, the localization of the various cations in the structure is complicated by the fact that the backscattering wave from  $\text{Al}^{3+}$  is

masked by destructive interference with backscattering waves from the heavier  $M^{2+}$  (Manceau, 1990; Scheinost *et al.*, 1999). Duan & Evans (2006) provide a summary of a variety of applications and problems concerning LDH phases.

For Zn–Al LDH, where part of the  $\text{Zn}^{2+}$  cations are replaced by  $\text{Al}^{3+}$  cations, we could demonstrate by wavelet analysis the presence of both types of atoms at distances of 3.06–3.08 Å from the Zn absorber atom (Funke *et al.*, 2005).

A second interesting feature of the LDH structure is the composition of the two metal shells at about 5.3 Å and 6.2 Å (see Fig. 1). If one assumes a regular distribution of  $\text{Al}^{3+}$  occupying one-third of all metal centers, then the 5.3 Å shell should contain only Zn atoms and the 6.2 Å shell should contain both Zn and Al atoms (Brindley & Kikkawa, 1979).

Fig. 2 shows the measured EXAFS spectrum of a Zn–Al LDH and its Fourier transform. The presence of  $\text{Zn}^{2+}$  and/or

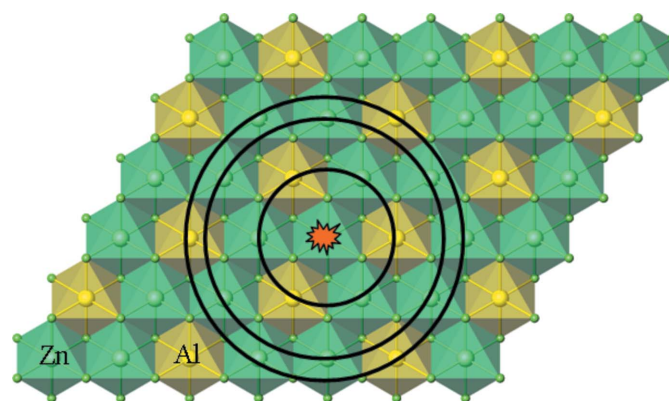


**Figure 1**  
Model of the octahedral layer of Zn–Al LDH.  $\text{Zn}(\text{OH})_6$  octahedra are shown in green (or dark grey),  $\text{Al}(\text{OH})_6$  octahedra are shown in yellow (or light grey). The circles mark the first three metal shells. This figure is in color in the electronic version of the paper.

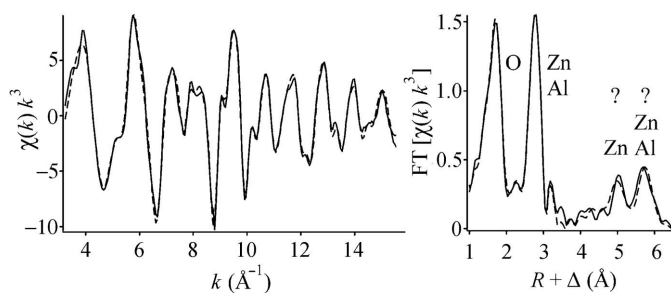


**Figure 2**  
Zn K-edge EXAFS spectrum and Fourier-transform magnitude of Zn–Al LDH. The fit is shown in dotted lines.

Al<sup>3+</sup> at the Fourier peaks labeled with question marks is not clear.

Our previous approach of employing the Morlet mother wavelet as a kernel of the wavelet transform was not suited to providing the necessary resolution in both  $k$  and  $r$  space to resolve both shells in distance and in atom type. Therefore, we developed a new kind of wavelet particularly for EXAFS data analysis, providing better resolution in both  $k$  and  $r$  space.

## 2. Wavelet transform for EXAFS analysis (Funke *et al.*, 2005)

The wavelet transform is a two-dimensional integral transform, which reaches a maximum when the wavelet (the kernel) of the transform coincides with the signal itself. *Vice versa*, the result is zero if there is no coincidence between the signal and the integral transform kernel. In analogy, the modulus of the one-dimensional Fourier transform shows maxima for such frequencies of the sine function, which are also contained in the signal.

The wavelet transform of the  $k^n$ -weighted EXAFS spectrum is given as

$$W_{\chi}^{\psi}(k, r) = (2r)^{1/2} \int_{-\infty}^{+\infty} \chi(k') k'^n \psi^*[2r(k' - k)] dk'. \quad (1)$$

Thereby the ‘mother’ wavelet function may be chosen from the wide class of functions  $l^2$  with zero mean as the only restriction,

$$\int_{-\infty}^{+\infty} \psi(k) dk = 0. \quad (2)$$

$\chi(k)$  is the EXAFS signal and  $\psi^*[2r(k' - k)]$  is the complex conjugated wavelet function, translated by  $k$  and dilatated by the parameter  $2r$ .

For EXAFS data analysis we have chosen the complex Morlet wavelet (Fig. 3). The Morlet wavelet is obtained by taking a complex sine wave (like in the Fourier transform) and by confining it with a Gaussian (bell-shaped) envelope,

$$\psi(k) = \frac{1}{(2\pi)^{1/2} \sigma} \exp(i\eta k) \exp(-k^2/2\sigma^2). \quad (3)$$

The parameter  $\eta$  is the frequency of the sine and cosine functions, determining how many oscillations of the sine wave are covered by a Gaussian envelope with the half width  $\sigma = 1$ .

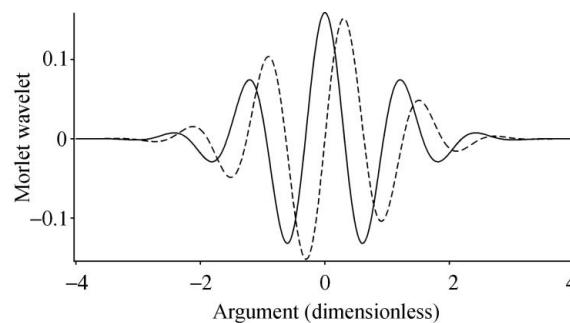


**Figure 3**  
Real (full line) and imaginary (dashed line) part of the Morlet wavelet for  $\eta = 5$  and  $\sigma = 1$ .

If the Morlet parameters fulfill the condition  $\eta\sigma \gg 10$ , *i.e.* if one forms a wavelet containing many oscillations (the ‘overview wavelet’), the dilatation parameter  $r$  of the wavelet transform and the distance parameter  $R$  of the Fourier transform coincide asymptotically. For Morlet parameters of the order of  $\eta\sigma \simeq 5$  (the ‘detail wavelet’), we receive a better resolution concerning the wavevector  $k$ .

The choice of the Morlet wavelet was based on the fact that its structure is similar to an EXAFS signal with a slowly varying amplitude term and a fast oscillating phase term. The parameters  $\eta$  and  $\sigma$  are sufficiently descriptive to be adapted easily to the present problem, *e.g.* to identify different elements at a given distance of the central atom.

The wavelet approach using Morlet wavelets is applied to resolve the Zn and Al atoms in the structure of Zn–Al LDH. The results are demonstrated in Figs. 4 and 7.

The wavelet ridge at  $r \simeq 2.65 \text{ \AA}$  shows two peaks at different  $k$ , the one at  $k \simeq 6.7 \text{ \AA}^{-1}$  corresponding to the Al backscattering, and the other at  $k \simeq 9.4 \text{ \AA}^{-1}$  corresponding to the Zn backscattering. Both backscatterers are at the same distance.

## 3. Limitations of the resolution using Morlet wavelets

Similar to a Gaussian normal distribution, where the information uncertainty, *i.e.* the resolution, is described by the half width  $\sigma$ , the wavelet transform distributes the information of the signal over some  $k$ – $r$  cells, so-called Heisenberg boxes (Chui, 1992; Louis *et al.*, 1997). The width of these cells is

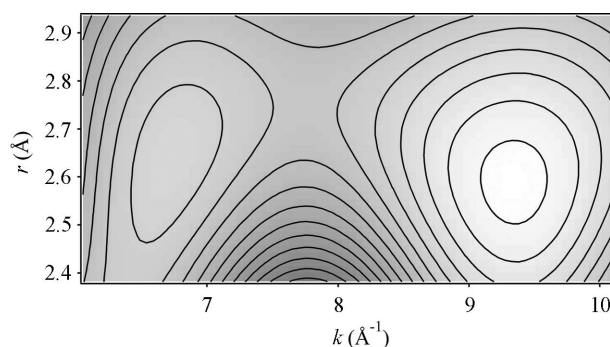


**Figure 4**  
Detail wavelet transform of the first metal shell with Morlet parameters  $\eta = 30$ ,  $s = 0.184$ .

defined by the second moments of the wavelet, for instance with reference to  $k$ ,

$$\Delta_{\psi}^k = \left[ \frac{1}{\|\psi\|^2} \int_{-\infty}^{+\infty} k^2 |\psi(k)|^2 dk \right]^{1/2} \quad (4)$$

where

$$\|\psi\|^2 = \int_{-\infty}^{+\infty} |\psi(k)|^2 dk.$$

Both widths ( $k$  and  $r$ ) of the cells depend on the chosen wavelet. The resolution properties of the wavelet transform are determined by the size of the corresponding uncertainty cell.

For the Morlet wavelet [equation (3)] the Heisenberg boxes  $[k \pm \Delta k] \times [r \pm \Delta r]$  have the form

$$\left[ k \pm \frac{\eta\sigma}{2^{1/2}r} \right] \times \left[ r \pm \frac{r}{2^{1/2}\eta\sigma} \right]. \quad (5)$$

It follows from relation (5) that the  $k$ - $r$  window is narrow in  $k$  space for large values of  $r$ , and is wide for small  $r$ . The resolution in  $r$  space hence decreases with increasing  $r$ . On the other hand, for large values of the product of the Morlet

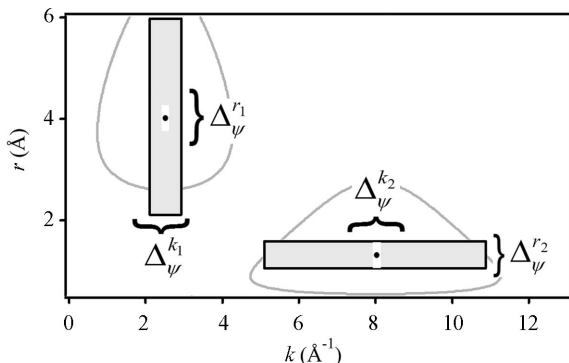


Figure 5 Two typical uncertainty cells (schematic).

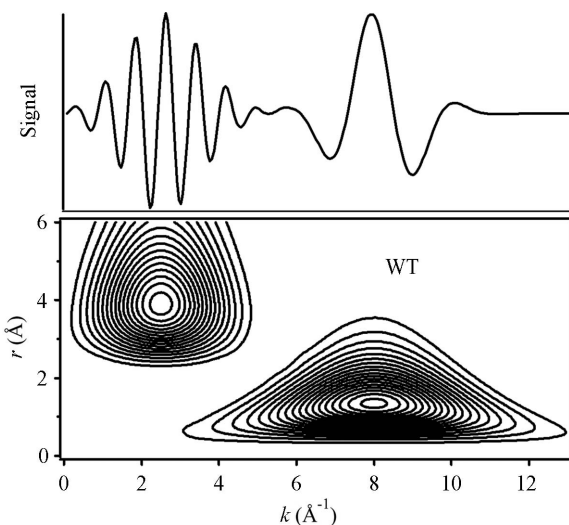


Figure 6 Model function with distances  $r_1 = 4.0 \text{ \AA}$  and  $r_2 = 1.3 \text{ \AA}$  centered at  $k = 2.5 \text{ \AA}^{-1}$  and  $k = 8.0 \text{ \AA}^{-1}$  and their wavelet transform (WT).

Table 1

Resolution properties of the wavelet transform for the first, second and third metal shells.

	$r_{\text{median}}$	$\eta\sigma$	$(k_{\text{max}} - k_{\text{min}})/2$	$(r_{\text{max}} - r_{\text{min}})/2$	$\eta\sigma/(2^{1/2}r)$	$r/(2^{1/2}\eta\sigma)$
First metal shell	2.65	5.52	2.00	0.40	1.47	0.34
Second + third metal shells (overview)	5.40	30	1.50	0.60	3.93	0.13
Second + third metal shells (detail)	5.40	4.65	0.75	0.60	0.61	0.82

parameters  $\eta\sigma$  the uncertainty is large for  $k$  and small for  $r$  and *vice versa*. Therefore, the resolution in  $k$  and  $r$  critically depends on the selection of the Morlet parameters  $\eta$  and  $\sigma$ . The Heisenberg uncertainty condition  $\Delta_k \Delta_r \geq 1/2$  [see equation (3.2.17) in Chui (1992)] is fulfilled by  $\Delta_k \Delta_r = 1/2$ .

To demonstrate exemplarily the effect of the resolution properties on wavelet transform plots, Fig. 5 shows two typical uncertainty cells with the centers  $k = 2.5 \text{ \AA}^{-1}$ ,  $r = 4 \text{ \AA}$  and  $k = 8 \text{ \AA}^{-1}$ ,  $r = 1.3 \text{ \AA}$ . The surface of both cells is equal.

The model function corresponding to Fig. 5,

$$f^{\text{mod}}(k) = \frac{1}{(2\pi)^{1/2}} \left\{ \sin(2 \cdot 4k) \exp[-(k - 2.5)^2/2] + \sin(2 \cdot 1.3k) \exp[-(k - 8)^2/2] \right\}, \quad (6)$$

and its wavelet transform are plotted in Fig. 6. The Morlet parameters are  $\eta = 7.5$  and  $\sigma = 0.5$ .

Qualitative knowledge of the behavior of the uncertainty boxes is indispensable for a deeper understanding of the wavelet transform of EXAFS data. The resolution conditions which follow from (5),

$$\frac{\eta\sigma}{2^{1/2}r} < \frac{k_{\text{max}} - k_{\text{min}}}{2} \quad \text{and} \quad \frac{r}{2^{1/2}\eta\sigma} < \frac{r_{\text{max}} - r_{\text{min}}}{2}, \quad (7)$$

were applied to the examples presented in Figs. 4 and 7 (see Table 1). The results show that the resolution conditions for  $k$  and  $r$  are both fulfilled for the first metal shell. For the second and third metal shell, however, the resolution condition is fulfilled either only for  $r$  in the overview wavelet transform or only for  $k$  in the detail wavelet. That means that the wavelet transform of the first metal shell consists of two single wavelet ridges separated in  $k$  and  $r$ , representing the two different types of atoms (Al, Zn). This is not the case for the overview and detail wavelet transform of the second and third metal shell. The overview wavelet transform shows two shells clearly discriminated in  $r$  in complete agreement with the Fourier transform (see Fig. 2), while the resolution is not sufficient to resolve the two types of atoms. In reverse, the detail wavelet transform shows two shells clearly discriminated in  $k$ , but the resolution is not sufficient to resolve the two different distances. Hence the simultaneous resolution in  $r$  and  $k$  space of the second and third metal shells is impossible using the Morlet wavelet. To overcome this limitation we have developed a new approach, which is described in the following sections.

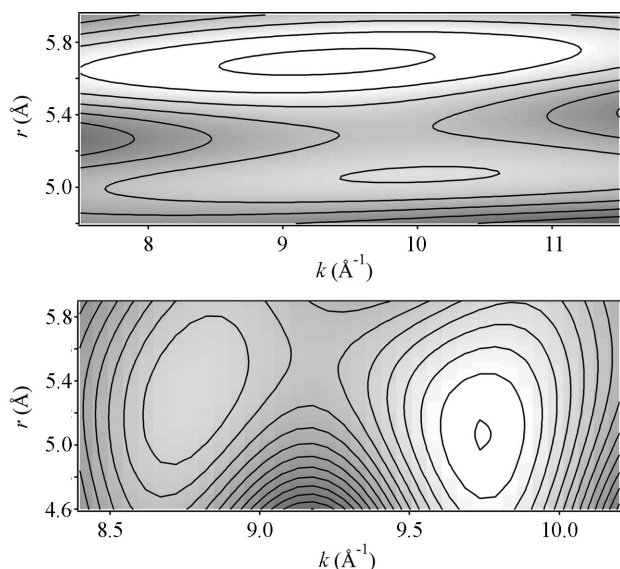


**Figure 7** Overview and detail wavelet transform of the second and third metal shells with Morlet parameters  $\eta = 30$ ,  $s = 1$  at the top and  $\eta = 30$ ,  $s = 0.155$  at the bottom.

#### 4. Construction of the *FEFF*–Morlet wavelet

When analyzing complex signals with wavelet transform, we have to discriminate two cases. In case one, neither a basic theory nor a mathematical model exist that could be applied to the process under investigation (e.g. Chui, 1992; Mallat, 2001; Daubechies, 1992). An example is the EEG signals of the human brain, where time–frequency plots of the electrical current measured in response to different events are treated as fingerprints of these events. Even without a basic theory, this wavelet method is widely used for medical diagnostics and has largely replaced Fourier analysis (e.g. Samar *et al.*, 1999). In case two, an at least rudimentary mathematical model of the process under investigation exists. The model, or parts of it, may then be used to construct a wavelet specifically adapted to the process. An example is seismic oil prospection, where the reflection of pressure waves on single sediment boundaries can be modeled, while the description of the complex reflection processes across greater depths of the Earth’s crust fails (Morlet *et al.*, 1982*a,b*; Kumar & Fofoula-Georgiou, 1997).

EXAFS spectra can be considered as belonging to this second group, since the spectra may be modeled by the so-called EXAFS equation, which is based on Fermi’s Golden Rule (e.g. Sayers & Stern, 1971; Stern, 1974; Lytle *et al.*, 1975; Stern *et al.*, 1975),

$$\chi(k) = S_0 \sum_{i=1}^n \frac{N_i F_i(k, R)}{R_i^2 k} \exp(-2R_i/\lambda) \exp(-2\sigma_i^2 k^2) \times \sin(2kR_i + \Psi), \quad (8)$$

where  $\chi(k)$  is the measured EXAFS spectrum and  $k$  is the electron wavevector. The searched, *i.e.* fitted, parameters are the number of atoms in the  $i$ th coordination sphere  $N_i$ , the average radial distance  $R_i$  and the Debye–Waller factor  $\sigma_i^2$ . The function’s backscattering amplitude,  $F_i(k, R)$ , the sum of

the phases of the central- and back-scattering atoms  $\Psi(k, R)$ , and the mean free path  $\lambda(k)$  are usually calculated using the *FEFF* code (Ankudinov *et al.*, 1998).

*FEFF* is a complex computer program for *ab initio* scattering calculations of EXAFS spectra using predetermined model clusters of atoms. The code yields theoretical scattering amplitudes and phases used in the standard XAFS analysis codes, as well as the EXAFS spectra for each path individually. The identity of the backscattering atom is not fitted and has to be pre-selected based on the underlying model.

In our new model, EXAFS functions for selected paths calculated using the *FEFF8.2* program (Ankudinov *et al.*, 1998) form the basis for the construction of mother wavelet functions. Wavelets designed in this way should be in good agreement with individual paths of interest, which are contained in the experimental spectrum. Thus the sensitivity of the wavelet transform for these paths is strengthened. In comparison with such real functions, complex mother wavelet functions, like Morlet or Cauchy wavelets, generate much more descriptive plots of magnitude. Thus, taking the *FEFF*-designed wavelet as the real part, the associated imaginary part has to be constructed. The sum of the real and the imaginary parts form the *FEFF*–Morlet wavelet. This wavelet is expected to combine the accurate characteristics of the theoretical EXAFS function with the descriptiveness and simplicity of the complex Morlet wavelet.

In the following sections, two tools are introduced which render the data analysis by means of wavelet transform more precise and more descriptive: the scale parameter  $s$  and the power density function.

#### 4.1. Four steps to the *FEFF*–Morlet wavelet

**4.1.1. Modeling a spectrum using *FEFF*.** An *FEFF* input file is written with one backscatterer atom at the distance of interest. The global Debye–Waller factor and the distance are taken from first fit estimations or from earlier results. The resulting `feff0001.chi` file,  $k^3$  weighted, is used as theoretical spectrum  $\chi^{\text{theor}}(k)$  (Fig. 8). The full  $\chi^{\text{theor}}(k)$  spectrum has to be restricted to its left-hand slope, *i.e.* the  $k$  interval which

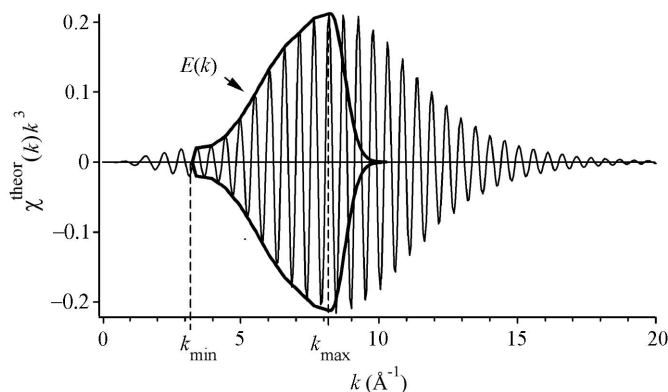


**Figure 8** Full model spectrum  $\chi^{\text{theor}}(k)k^3$  for Zn–Zn backscattering at 6.2 Å from *FEFF8.2*. The Debye–Waller factor is  $\sigma^2 = 0.0065 \text{ \AA}^2$ . The envelope  $E(k)$ , which is used for the construction of the *FEFF*–Morlet wavelet, is drawn in bold lines.

contains information on the amplitude function. The right-hand slope, *i.e.* the signal for large  $k$  values, is attenuated substantially by the Debye–Waller factor, and typical amplitude information is suppressed. In addition, the complete calculated  $\chi^{\text{theor}}(k)$  function contains too many oscillations, and a wavelet built from the full  $\chi^{\text{theor}}(k)$  would behave like an overview Morlet wavelet, *i.e.* would not be sensitive to the amplitude information. Therefore, the maximum of the envelope of the theoretical spectrum is chosen as the upper limit of the relevant  $k$  range,  $k_{\text{max}}$ , and the lower limit,  $k_{\text{min}}$ , is taken from the spectrum (see Fig. 8).

**4.1.2. Adjustment of the amplitude information.** The envelope  $E(k)$  is built by a spline procedure connecting the maxima of the oscillations of the spectrum (Fig. 8) between  $k_{\text{min}}$  and  $k_{\text{max}}$ . To avoid truncation effects in the wavelet transform, the envelope is smoothed by adding the right-hand half of a Gaussian curve with half width  $\sigma = 1/2 \text{ \AA}$ . The resulting model spectrum in the limits  $k_{\text{min}}$  and  $k_{\text{max}}$  complemented by the smoothing function attached to the right-hand side of  $k_{\text{max}}$  is  $\chi^{\text{mod}}(k)$ .

**4.1.3. Adjustment of the phase information of  $\chi^{\text{mod}}(k)$ .** Knowing the envelope  $E(k)$ , the real part of a complex function  $\psi(k)$  (the future *FEFF*–Morlet wavelet) is defined as

$$\text{Re } \psi(k) = E(k) \cos(2kr + \varphi). \quad (9)$$

The values of the parameters in the cosine function, distance (frequency)  $r$  and phase  $\varphi$ , will be adapted from  $\chi^{\text{mod}}(k)$  by means of a correlation procedure. We calculate the correlation function  $C(r, \varphi)$  between the functions  $\text{Re } \psi(k)$  and  $\chi^{\text{mod}}(k)$  with respect to a unique distance (frequency)  $r$  and phase  $\varphi$ ,

$$C(r, \varphi) = \int_{k_{\text{min}}}^{k_{\text{max}}} E(k) \cos(2kr + \varphi) \chi^{\text{mod}}(k) dk. \quad (10)$$

Thereby the values of  $r$  and  $\varphi$  are varied in the ranges  $r \in [r + \delta r, r - \delta r]$  ( $\delta r < 0.5 \text{ \AA}$ ) and  $\varphi \in [0, 2\pi]$ , fulfilling  $C(r, \varphi) \rightarrow \text{max}$ .  $\delta r$  must be selected in such a way that no influence of a neighbor shell exists.

The imaginary part of the *FEFF*–Morlet wavelet is then simply built by addition of a phase shift of  $\pi/2$  to the phase of  $\text{Re } \psi(k)$  with the implicit understanding that  $E(k)$  is a real function,

$$\text{Im } \psi(k) = E(k) \sin(2kr + \varphi). \quad (11)$$

**4.1.4. Fulfilling the ‘zero mean’ condition.** The complex function  $\psi(k)$  has to be converted into a mother wavelet, fulfilling the condition (2). That means that we translate  $\psi(k)$  on the  $k$  axis by a correction  $k_{\text{grav}}$  and add a phase correction  $\varphi$  such that the center of gravity becomes zero. With this final step, the *FEFF*–Morlet (FM) wavelet is fully defined,

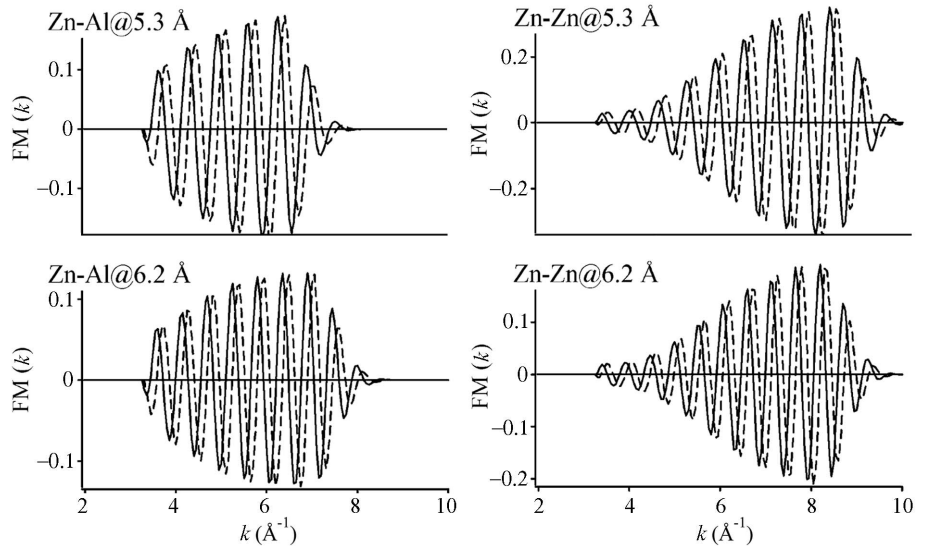


**Figure 9** Real (full lines) and imaginary (dashed lines) part of the *FEFF*–Morlet wavelets  $FM(k)$  constructed from the four model spectra.

$$\begin{aligned} \text{Re } \psi^{\text{FM}}(k) &= E(k + k_{\text{grav}}) \cos[2(k + k_{\text{grav}})r + \varphi], \\ \text{Im } \psi^{\text{FM}}(k) &= E(k + k_{\text{grav}}) \sin[2(k + k_{\text{grav}})r + \varphi]. \end{aligned} \quad (12)$$

The resulting *FEFF*–Morlet wavelets based on the single scattering paths Zn–Al at 5.3 and 6.2  $\text{Å}$  with the Debye–Waller factor  $\sigma^2 = 0.0056 \text{ \AA}^2$ , and Zn–Zn at 5.3 and 6.2  $\text{Å}$  with  $\sigma^2 = 0.0065 \text{ \AA}^2$ , are shown in Fig. 9.

## 4.2. From distance ( $r$ ) to scale parameter ( $s$ )

As noted in the *Introduction*, the magnitude of an integral transform has a maximum if the agreement of the integral kernel (wavelet) and the signal is at a maximum. To express this fact more descriptively, the wavelet transform for EXAFS analysis [equation (1)] is reformulated in an adequate way. Owing to its construction, the *FEFF*–Morlet wavelet is the optimal mother wavelet function for a specific backscattering atom at a specific distance. The information about the optimal distance is contained in the *FEFF*–Morlet wavelet  $\psi_{[r_{\text{opt}}]}^{\text{FM}}$  itself. Each scaling (stretching or shrinking) would mean a decrease of the agreement, if the basis model is correct.

Consequently, the dilatation parameter  $r$  is replaced by a new scale parameter  $s$  if the mother wavelet is a function derived from a certain model. *The definition of  $s$  is that  $s = 1$  if the argument of the wavelet is not scaled.* This means that, if the wavelet transform for  $s = 1$  (in a certain region of  $k$ ) shows a maximum, then the signal and the mother wavelet function in this  $k$  region coincide maximally. It is reminded that the dilatation parameter  $r$  (like the distance parameter  $R$  of the Fourier transform) is not phase corrected. However, the meaning of  $s$  is clearly defined.

The wavelet transform, depending on the translation and scale parameters  $k$  and  $s$ , then takes the form

$$W_{\chi}^{\psi}(k, s) = s^{1/2} \int \chi(k') k'^3 \psi_{[r_{\text{opt}}]}^{\text{FM}*}[s(k' - k)] dk'. \quad (13)$$

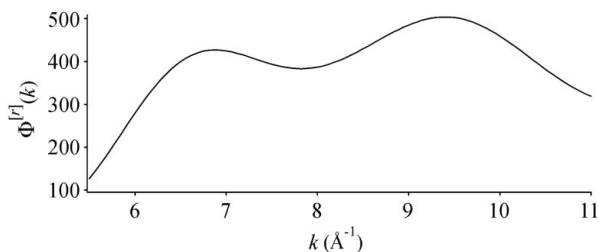


**Figure 10**  
PDF  $\Phi(k)$  of the detail wavelet transform for the first metal shell (see Fig. 4) within the limits  $r_1 = 2.5 \text{ \AA}$  and  $r_2 = 2.75 \text{ \AA}$ .

For each value of  $s$ , the wavelet transform with respect to  $k$  reduces to a convolution of  $\chi(k)k^3$  with  $\psi_{[r_{\text{opt}}]}^{\text{FM}^*}$ . Consequently, the relation between the scale parameter  $s$  and the physical parameter  $r$  is wavelet dependent.

### 4.3. The power density function

In order to focus the wavelet transform analysis to specific distances and specific  $k$  ranges, the power density function (PDF)  $\Phi$  is introduced depending on either  $k$ ,  $s$  or  $r$ . Thereby the computation of  $\Phi(k)$  is performed by integration over a distance range  $\Delta r$  or  $\Delta s$ . The computation of  $\Phi(s)$  and  $\Phi(r)$  is performed by integration over the entire  $k$  range of the experimental spectrum,

$$\Phi^{[s]}(k) = \int_{s_1}^{s_2} [W_{\chi}^{\psi}(k, s)]^2 ds, \quad (14)$$

$$\Phi^{[r]}(k) = \int_{r_1}^{r_2} [W_{\chi}^{\psi}(k, r)]^2 dr,$$

$$\Phi(s) = \int_{k_{\text{min}}}^{k_{\text{max}}} [W_{\chi}^{\psi}(k, s)]^2 dk, \quad (15)$$

$$\Phi(r) = \int_{k_{\text{min}}}^{k_{\text{max}}} [W_{\chi}^{\psi}(k, r)]^2 dk.$$

An example of a PDF  $\Phi(k)$  resolving two backscattering centers at  $r \simeq 2.65 \text{ \AA}$  is shown in Fig. 10 (compare with Fig. 4).

Analysis of the function  $\Phi(k)$  is useful if the  $k$  resolution of the wavelet ridges in simple contour plots is not easy to interpret. An application of  $\Phi(s)$  will be given in the following section.

## 5. Application of wavelet analysis to the second and third metal shell of the Zn–Al LDH

The *FEFF*–Morlet technique is applied to verify the model of Brindley & Kikkawa (1979), assuming an even metal distribution in the LDH layer, in line with an even charge distribution. In this case the first metal shell ( $r \simeq 3.1 \text{ \AA} = R_{\text{Zn-Zn}}$ ) contains three Zn and three Al atoms, the second metal shell ( $r \simeq 5.3 \text{ \AA} = 3^{1/2}R_{\text{Zn-Zn}}$ ) contains six Zn atoms, and the third metal shell ( $r \simeq 6.2 \text{ \AA} = 2R_{\text{Zn-Zn}}$ ) contains three Zn and three Al atoms.

Now the wavelet transform analysis of the second and third metal shell of the LDH spectrum will be performed using the

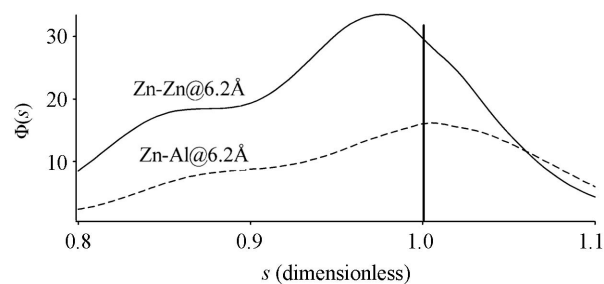


**Figure 11**  
Two PDFs  $\Phi(s)$  of the wavelet transform of Zn–Al LDH, performed using the adapted *FEFF*–Morlet wavelets (see text).

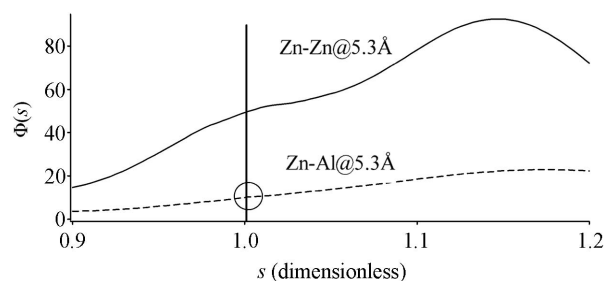


**Figure 12**  
Two PDFs  $\Phi(s)$  of the wavelet transform of Zn–Al LDH, performed using the adapted *FEFF*–Morlet wavelets (see text).

following four *FEFF*–Morlet wavelet mother functions (Fig. 9): Zn–Zn at  $6.2 \text{ \AA}$ , Zn–Al at  $6.2 \text{ \AA}$ , Zn–Zn at  $5.3 \text{ \AA}$  and Zn–Al at  $5.3 \text{ \AA}$ . The start functions  $\chi^{\text{mod}}(k)$  were calculated using the *FEFF* program, and the final wavelets were designed following the procedure described in §4.

For  $r \simeq 6.2 \text{ \AA}$ , the analysis of the wavelet transforms with the power density function  $\Phi(s)$  shows maxima around  $s = 1$  for Zn and Al, confirming that both atoms are present at this distance (Fig. 11). At a distance of  $r \simeq 5.3 \text{ \AA}$ , however, only the path involving Zn backscattering shows an additional shoulder at  $s = 1$ , while the path involving Al does not (circle) (Fig. 12). This confirms the model shown in Fig. 1.

## 6. Conclusions

It is demonstrated that a wavelet analysis of EXAFS data using a combined *FEFF*–Morlet wavelet is able to discriminate different atoms at similar distances when the resolution of the Morlet wavelet is not sufficient. With the previously used Morlet wavelet, it was possible to distinguish Zn and Al in the first metal shell ( $3.1 \text{ \AA}$ ) of the LDH spectrum. However, it was not possible to resolve the two more distant shells at  $5.3$  and  $6.2 \text{ \AA}$  simultaneously with respect to wavenumber  $k$  (element identity) and distance  $r$ . This problem is now overcome with the newly developed *FEFF*–Morlet wavelet. *FEFF*–Morlet wavelets were individually adapted to resolve the second and third metal shell of Zn–Al LDH. In confirmation of Brindley & Kikkawa’s model (Brindley & Kikkawa, 1979) postulating an even charge distribution in LDHs, we were now able to show that the second metal shell contains only Zn, and the third metal shell contains both Zn and Al.

In this study we made use of the most important advantage of the continuous wavelet transform, the possibility to permit infinitely many test functions from the function class  $l^2$ . The *FEFF*-Morlet wavelet is a sharper, though more complicated, instrument for EXAFS data analysis compared with the Morlet wavelet.

This work is supported by the NATO Collaborative Linkage Grant CBPNR.CLG 981353. M. Chukalina thanks the Russian Foundation for Basic Research (RFBR 05-01-00984-A) for additional support.

### References

- Ankudinov, A. L., Ravel, B., Rehr, J. J. & Conradson, S. D. (1998). *Phys. Rev. B*, **58**, 7565–7576.
- Brindley, G. W. & Kikkawa, S. (1979). *Am. Mineral.* **64**, 836–843.
- Chui, C. K. (1992). *An Introduction to Wavelets*. San Diego/London: Academic Press.
- Daubechies, I. (1992). *Ten Lectures on Wavelets*. Philadelphia: SIAM.
- D’Espinose, J. B., Kermarec, M. & Clause, O. (1995). *Am. Chem. Soc.* **117**, 11471–11481.
- Duan, X. & Evans, D. G. (2006). Editors. *Structure and Bonding*, Vol. 119, *Layered Double Hydroxides*. Berlin/Heidelberg: Springer.
- Funke, H., Scheinost, A. C. & Chukalina, M. (2005). *Phys. Rev. B*, **71**, 094110.
- Harfouche, M., Wieland, E., Dähn, R., Fujita, T., Tits, J., Kunz, D. & Tsukamoto, M. (2006). *J. Colloid Interface Sci.* **303**, 195–204.
- Kumar, P. & Fofoula-Georgiou, E. (1997). *Rev. Geophys.* **35**, 385–412.
- Louis, A. K., Maas, P. & Rieder, A. (1997). *Wavelets: Theory and Applications*. New York: Wiley.
- Lytle, F. W., Sayers, D. E. & Stern, E. A. (1975). *Phys. Rev. B*, **11**, 4825–4835.
- Mallat, S. (2001). *A Wavelet Tour of Signal Processing*. San Diego/London: Academic Press.
- Manceau, A. (1990). *Can. Mineral.* **28**, 321–328.
- Morlet, J., Arens, G., Fourgeau, E. & Giard, D. (1982a). *Geophysics*, **47**, 203–221.
- Morlet, J., Arens, G., Fourgeau, E. & Giard, D. (1982b). *Geophysics*, **47**, 222–236.
- Muñoz, M., Argoul, P. & Farges, F. (2003). *Am. Mineral.* **88**, 694–700.
- Sahnoun, M., Daul, C. & Haas, O. (2007). *J. Appl. Phys.* **101**, 014911.
- Samar, V. J., Bopardikar, A., Rao, R. & Swartz, K. (1999). *Brain Lang.* **66**, 7–60.
- Sayers, D. E. & Stern, E. A. (1971). *Phys. Rev. Lett.* **27**, 1204–1207.
- Scheinost, A. C., Ford, R. G. & Sparks, D. L. (1999). *Geochim. Cosmochim. Acta*, **63**, 3193–3203.
- Stern, E. A. (1974). *Phys. Rev. B*, **10**, 3027–3037.
- Stern, E. A., Sayers, D. E. & Lytle, F. W. (1975). *Phys. Rev. B*, **10**, 4836–4846.
- Vespa, M., Daehn, R. D., Grolimund, D., Wieland, E. & Scheidegger, A. M. (2006). *Environ. Sci. Technol.* **40**, 2275–2282.
- Voegelin, A., Scheinost, A. C., Bühlmann, K., Barmettler, K. & Kretzschmar, R. (2002). *Environ. Sci. Technol.* **36**, 3749–3754.